nature communications

Article

https://doi.org/10.1038/s41467-024-52226-4

Unveiling crystal orientation-dependent interface property in composite cathodes for solid-state batteries by in situ microscopic probe

Received: 8 February 2024

Accepted: 27 August 2024

Published online: 11 September 2024

Check for updates

Sunyoung Lee[1,7], Hayoung Park[2,3,7], Jae Young Kim[1], Jihoon Kim[2,3], Min-Ju Choi[1], Sangwook Han[1], Sewon Kim[1,4], Wonju Kim[1], Ho Won Jang[1,5], Jungwon Park[2,3,5,6] ✉ & Kisuk Kang[1,2,3,6] ✉

A critical bottleneck toward all-solid-state batteries lies in how the solid(electrode)-solid(electrolyte) interface is fabricated and maintained over repeated cycles. Conventional composite cathodes, with crystallographically distinct electrode/electrolyte interfaces of random particles, create complexities with varying (electro)chemical compatibilities. To address this, we employ an epitaxial model system where the crystal orientations of cathode and solid electrolyte are precisely controlled, and probe the interfaces in real-time during co-sintering by in situ electron microscopy. The interfacial reaction is highly dependent on crystal orientation/alignment, especially the availability of open ion channels. Interfaces bearing open ion paths of NCM are more susceptible to interdiffusion, but stabilize with the early formed passivation layer. Conversely, interfaces with closed ion pathway exhibit stability at intermediate temperatures, but deteriorate rapidly at high temperature due to oxygen evolution, increasing interfacial resistance. The elucidation of these distinct interfacial behaviors emphasizes the need for decoupling collective interfacial properties to enable rational design in solid-state batteries.

All-solid-state batteries (ASSBs) are considered potential game-changers in the transition to electric vehicles, owing to their superior safety features and the high energy density achievable through advanced system design[1–5]. The recent proliferation of ASSBs is largely attributed to the discovery of various sulfide-, oxide- and halide-based solid electrolyte materials which could exhibit lithium ionic conductivities that are comparable to those of commercial liquid electrolytes in lithium-ion batteries[3,4,6]. Furthermore, the ionic transport in these solid electrolytes often benefits from a high transference number of lithium-ions, offsetting their slightly lower ionic conductivity[3,4]. However, despite the considerable advancements in solid electrolyte materials, their employment in practical ASSBs has been hampered by difficulties particularly in securing the reliable interface between the solid electrolyte and the electrode. The compatibility between the two should be satisfied not only in physical intactness but also in chemical and electrochemical stability. Moreover, this integrity should be

[1]Department of Materials Science and Engineering, Seoul National University, Seoul 08826, Republic of Korea. [2]School of Chemical and Biological Engineering, Institute of Chemical Process, Seoul National University, Seoul 08826, Republic of Korea. [3]Center for Nanoparticle Research, Institute for Basic Science (IBS), Seoul National University, Seoul 08826, Republic of Korea. [4]Next Generation Battery Lab, Samsung Advanced Institute of Technology, 130, Samsung-ro, Yeongtong-gu, Suwon-si, Gyeonggi-do 443-803, Republic of Korea. [5]Advanced Institute of Convergence Technology, Seoul National University, Suwon 16229, Republic of Korea. [6]Institute of Engineering Research, College of Engineering, Seoul National University, Seoul 08826, Republic of Korea. [7]These authors contributed equally: Sunyoung Lee, Hayoung Park. ✉e-mail: jungwonpark@snu.ac.kr; matlgen1@snu.ac.kr

guaranteed not only during the fabrication process but also throughout the dynamic electrochemical cycling, which involves continuous changes of the active electrode material with respect to the physical volume/shape and chemical states arising from different states of charges (SOCs).

In response to these challenges, various strategies have been devised in recent years such as applying external pressure to constantly ensure physical contact or coating active materials to stabilize the interface[1,5–8]. While some success was witnessed especially for sulfide-based electrolytes that are mechanically malleable with the external pressure adjustment[5,7], it is questionable whether the additional pressure devices can be practically viable for commercial ASSBs. Moreover, these approaches are not eligible for oxide-based electrolytes (e.g., perovskite, NASICON, and garnet-type electrolytes)[2,9–12], which are typically rigid and fragile. The brittle mechanical properties of oxide electrolytes inherently result in inferior interfacial contact between particles in composite cathodes when fabricated at ambient temperature[13–16], thus requiring co-sintering process at high temperatures (e.g., above 1000 °C with the garnet-type[14–17], NASICON solid electrolyte[18–20], and perovskite[21,22]). However, these high-temperature treatments often exacerbate unwanted reactions at the interface, such as cation interdiffusion, interphase formation, and decomposition of coating materials, subsequently leading to a high-resistance interface. While numerous efforts have been made to optimize the processing conditions to mitigate the trade-off between sintering and side reactions, the results have been inconsistent and often limited in success even for identical materials[18–24].

In the fabrication of conventional composite cathodes, cathode active materials are mixed with solid electrolyte powders, and then sintered to ensure their interfacial contact. This process yields a composite cathode bearing complex interfaces among randomly distributed cathode and solid electrolyte particles. This randomness means various crystalline planes of the cathode may interface with solid electrolytes of differing orientations, creating a range of interfaces with diverse properties. Given that each crystalline plane may have unique reactivity, surface energy and transport properties, the formation mechanism/kinetics of the interface would be greatly varied and influenced during the sintering process. Moreover, these varied interfacial properties are crucial to the activity and stability of composite cathodes during electrochemical cycling, especially for cathode materials like layered lithium transition metal oxides and olivine cathodes, which exhibit anisotropic lithium-ion transport depending on crystalline planes[1,25–29]. However, probing these interfacial properties remains challenging due to their irregular structures and the occurrence of various side reactions[15–24,30–32]. Bulk analyses often provide limited insight and tend to overlook kinetically-driven intermediate states crucial to the overall reaction process[33,34]. Recent studies have begun exploring the influence of crystal facets of cathode materials on electrochemical performance by developing systems with controlled crystal orientations[1,25–27]. For instance, $LiCoO_2$ with highly faceted (003) planes perpendicular to the substrate showed improved cycling performance compared to composites with random facets[1]. Despite these recent advancements, a detailed understanding of the interfacial reactions during co-sintering, particularly how crystallographic alignment affects the interaction between cathode and oxide solid electrolyte materials, remains elusive.

In this work, we attempt to unravel the complexity of the interface by exploring model interfacial systems in which the crystal orientations of cathode and electrolyte are precisely controlled through the epitaxial growth. Taking a representative layered cathode material $Li(Ni_{1/3}Co_{1/3}Mn_{1/3})O_2$ (NCM) and perovskite-type oxide solid electrolyte $Li_{3x}La_{(2/3)-x}\square_{(1/3)-2x}TiO_3$ (LLTO) system, we probe the formation mechanism of their interface by in situ heating transmission electron microscopy (TEM) and examine the resulting interfacial properties by electrochemical impedance spectroscopy (EIS). Two types of the epitaxial heterostructure of NCM/LLTO are fabricated; one without apparent ion diffusion channels between the cathode and electrolyte (i.e., closed ion pathway, NCM(003)/LLTO(112)), and the other with ion diffusion channels (i.e., open ion pathway, NCM(104)/LLTO(020)). Our comparative investigations reveal the crucial influence of the crystal orientation on the interfacial reaction and the charge transfer resistance. We demonstrate that interfaces featuring open ion paths are more prone to interdiffusion during the co-sintering process, even at low temperatures. However, the early formation of a stable passivation layer significantly mitigates the rise in overall interfacial resistance. Conversely, interfaces with closed ion pathways maintain relatively high stability up to intermediate temperatures during co-sintering. Yet, they undergo more rapid deterioration at high temperatures due to oxygen evolution and decomposition, and result in increased interfacial resistance, implying the importance of forming a partial buffer layer through a certain degree of cation interdiffusion. Our real-time probe of the well-defined interface opens up a new possibility in unraveling the complex interfacial properties in composite cathodes, offering insights into designing composite cathodes with stable interfaces for high-performance ASSBs.

Results

A crystal orientation-controlled NCM/LLTO model system

The perovskite-type LLTO is one of the most widely-studied solid electrolytes for its high ionic conductivity (10^{-4} ~ 10^{-3} S cm^{-1}) and chemical stability with high oxidation potential, thus was chosen for this investigation[11,21,22]. In the standard process of fabricating composite cathodes for ASSBs, a mixture of solid electrolyte and cathode active powders is co-sintered at high temperatures. In this context, we first examined the co-sintering behavior of the blended powder comprising of LLTO electrolyte and NCM cathode materials using in situ heating X-ray diffraction (XRD) under Ar atmospheres. (Fig. 1a) The in situ heating XRD under O_2 atmospheres was also conducted and discussed in Fig. S1. It shows that heating the mixture up to approximately 700 °C does not induce noticeable side reactions, only displaying the typical thermal expansion behavior with slight downshifts of the XRD peaks. However, the intensities of the LLTO and NCM peaks weakened with increasing sintering temperature further to 750 °C. Subsequently, a peak was detected at 22.7° (3.915 Å), which was found to correspond to $La(TM)O_3$ (TM, transition metal, e.g., $LaNi_{0.5}Ti_{0.5}O_3$) signifying side reactions occurring between LLTO and NCM. A similar $La(TM)O_3$ (TM = Ni, Mn, Co) phase was previously reported as an interfacial byproduct of garnet-type oxide solid electrolyte and layered cathode materials at 700–800 °C[30,35]. The evolution of NCM cathodes at high temperature depicted in the enlarged XRD patterns (Fig. 1b) reveals that a set of some peaks begins to evolve discontinuously, which match with the $LiTiO_2$ and disordered spinel-type NCM phase ($Fd\bar{3}m$, ICDD PDF 04-011–9609, as indicated with red color)[36]. Considering that a phase transition from layered to spinel is typically observed with a delithiated layered material at high temperature[37–39], it may indicate substantial lithium-ion diffusion from the cathode to the solid electrolyte[19]. To verify lithium-ion migration from the NCM to LLTO, we compared the electrolyte peaks between the NCM/LLTO mixture and LLTO alone. It revealed a transition where the electrolyte peaks shifted to lower angles at approximately 700 °C (Fig. S2). These observations contrast with the stable thermal behavior of individual LLTO samples, which maintained their original structures up to 850 °C.

Previous studies on the structural changes of LLTO indicate that when lithium ions insert into the vacancy sites of the electrolyte, the c lattice parameter increases, resulting in a transition from a tetragonal unit cell to two cubic unit cells[40,41]. The plot of LLTO unit cell volume changes as a function of temperature showed that the volume of LLTO increased from 118.55 $Å^3$ to 121.07 $Å^3$ at 700 °C, where the interfacial reaction was observed (Fig. S2c). This volume expansion upon lithium-ion insertion in the LLTO electrolyte is consistent with previous

https://doi.org/10.1038/s41467-024-52226-4

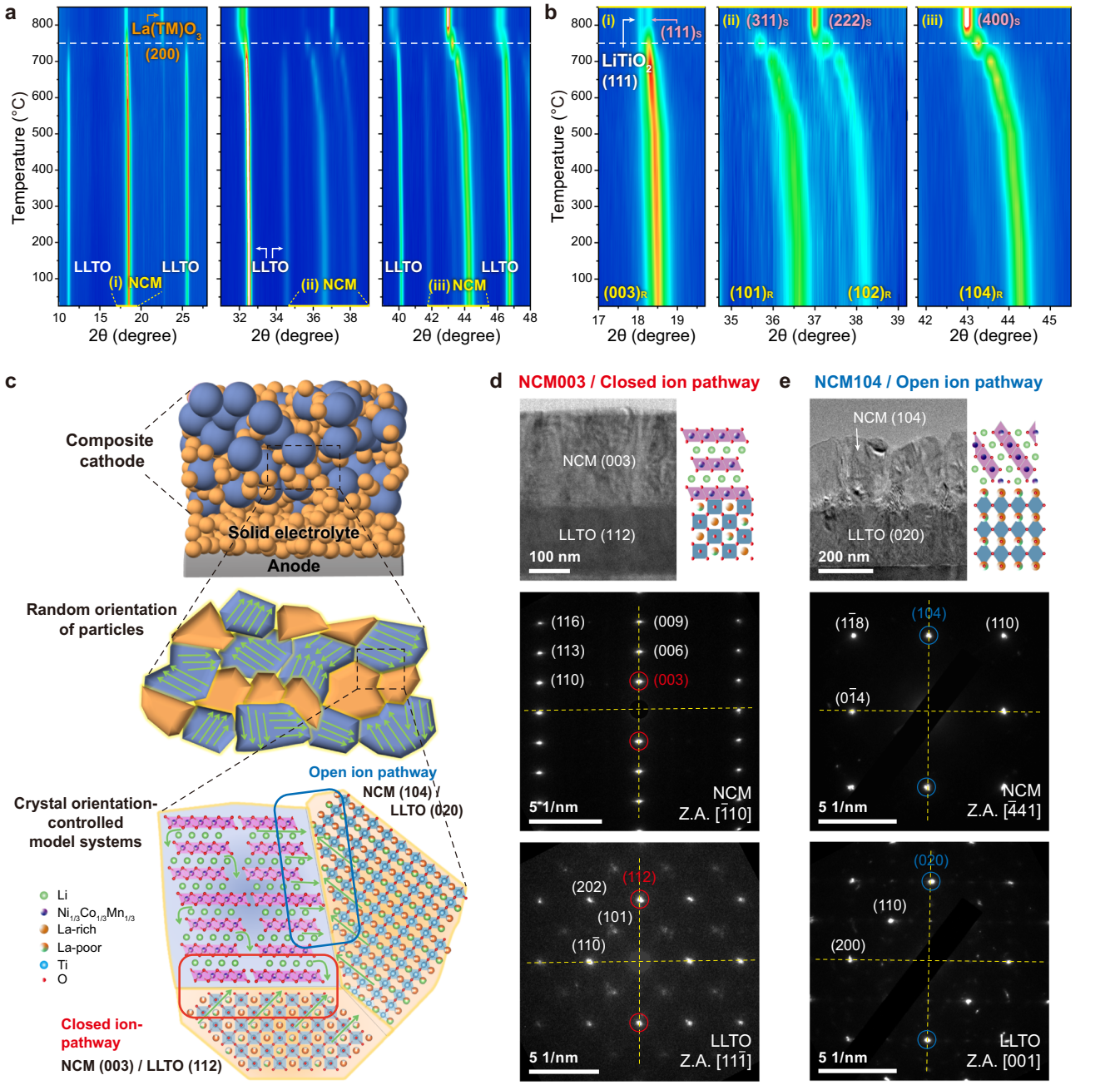

Fig. 1 | Crystal orientation-controlled model systems for understanding the interface between the cathode and the solid electrolyte in composite cathodes. **a** In situ heating XRD profiles of the NCM and LLTO powder mixture during heating up to 850 °C. The spinel phase and La(TM)O_3 phase are matched with ICDD PDF 04-011-9609 and PDF 00-069-0419, respectively. **b** The enlarged XRD patterns in the range of (i) 17–20 °, (ii) 35-39 °, and (iii) 41–46 ° are for NCM(003), (101), and (104), respectively. R represents the rhombohedral phase (R$\bar{3}$m) and S represents the spinel phase (Fd$\bar{3}$*m*). **c** Schematic illustration of the conventional composite cathodes and the crystal orientation-controlled model system. Two types of epitaxial growth as the model system are employed; open ion pathway and closed ion pathway. TEM images and NBD patterns of the epitaxial structure of NCM (003)/LLTO(112) (**d**) and NCM(104)/LLTO(020) (**e**) along each zone axis (Z.A.).

literatures. Therefore, both the phase transition of NCM to spinel and the volume increase of LLTO suggest the possibility of lithium-ion diffusion from NCM to LLTO. These observations contrast to the stable thermal behavior of individual LLTO and NCM samples, which maintained the original structures up to 850 °C, as presented in Fig. S3. It suggests that the co-sintering process at temperature over 750 °C may induce the deterioration of NCM/LLTO composite structure rather than the desired densification.

The composite cathode, a blend of cathode and solid electrolyte particles, features randomly oriented crystal facets that interface with each other, as illustrated in Fig. 1c. Consequently, the interfacial side reaction observed in Fig. 1a represents the cumulative effect of reactions at these individual interfaces. This is especially true for layered materials with anisotropic diffusion pathways of ions, where lithium-ions easily diffuse along the (003) plane, whereas their movement perpendicular to the (003) plane is significantly hindered[42,43]. In order to decouple this cumulative effect, we designed model interfacial systems using the epitaxial growth of materials on single-crystal substrates and investigated this orientation-dependent ion transport and thermal stability (bottom images in Fig. 1c). Among various interfacial orientations, two systems of NCM(003)/LLTO(112) and NCM(104)/LLTO(020) were selected as representative interfaces with closed ion

channels and open ion channels, respectively. The diffusion of lithium (or TM) ions is expected to be facile when the NCM(104) plane is exposed to the LLTO(020), while it is difficult when the electrolyte interface is blocked by the NCM(003) plane, as illustrated with blue and red boxes, respectively, in Fig. 1c. In the sample preparation, the LLTO solid electrolytes oriented along the [112] and [020] orientations were firstly grown on Nb-doped $SrTiO_3$ single crystal substrates with the [111] and [001] orientations, respectively. This was followed by the epitaxial growth of NCM(003) and NCM(104) planes on the corresponding LLTO(112) and LLTO(020) planes, a process facilitated by the similar oxygen ion arrangements between LLTO and NCM in these directions, making an ideal interface (See more details on the epitaxial film growth in the experimental section)[26,44]. Fig. 1d, e showcase the cross-sectional TEM images of the epitaxial NCM/LLTO systems, along with the selected area electron diffraction (SAED) patterns for NCM003 and NCM104, respectively. To simplify terminology, the NCM(003)/LLTO(112) and NCM(104)/LLTO(020) heterostructures are henceforth referred to as NCM003 and NCM104, respectively. These images confirm the successful growth of NCM materials on the designated LLTO substrates, representing the desired interface. Each SAED pattern distinctly reveals single crystalline patterns; NCM(003) planes and LLTO(112) planes are evident for NCM003 (marked with red dots in Fig. 1d), while NCM(104) and LLTO(020) planes are clearly visible in NCM104 (indicated with blue dots in Fig. 1e)[45–47], verifying the intended interfacial growth. The interface in NCM003 is notably flat with a clear boundary between NCM and LLTO, contrasting with the NCM104, which exhibits a relatively rough interface featuring island-like NCM(104) domains. This difference is attributed to the preferred growth kinetics along the (003) planes of typical layered oxides, a phenomenon also observed in previous studies of $LiCoO_2$ epitaxial growth[44]. Further analysis of the samples is provided in Fig. S4 in the supplementary section.

Probing the orientation-aligned interface real-time during co-sintering

We investigated the evolution of the aforementioned orientation-controlled interface during the co-sintering process of NCM/LLTO systems through in situ heating TEM. Specimens of NCM003 and NCM104, prepared via a focused-ion beam (FIB), were placed on a microchip for heating and incrementally heated to high temperature (refer to Fig. S5 for details). Fig. 2a presents a series of snapshot images from the movie (movie S1) taken for the NCM003 sample during the heating process. It reveals that NCM003, with its closed ion pathway, retains a distinct interface structure up to about 600 °C, while, beyond this temperature, the structural degradation becomes apparent at the interface as highlighted by the formation of bright contrast areas (dotted box along with the contrast image in the inset). These bright contrast areas were observed to further spread across the interface upon exposure to higher temperature, as more clearly depicted in movie S1. More interestingly, NCM104, characterized by an open ion pathway, shows interface changes starting at a considerably lower temperature. Fig. 2b and movie S2 illustrate that at as early as around 400 °C, the interfacial boundary becomes notably blurred, as evidenced by the color-coded images of the contrast change in the insets of the figure. However, these early deterioration features did not exacerbate significantly with further heating to higher temperatures. These observations suggest that the local interfacial degradation is initiated well before the macroscopic detection of interfacial byproducts becomes feasible with XRD in Fig. 1a.

In order to clarify the changes in the interface, we further conducted high-resolution ex situ TEM (HR-TEM) analysis on the NCM003 and NCM104 samples at their respective onset temperature of ~ 600 °C and ~ 400 °C. (The HR-TEM images of pristine interfaces are provided in Fig. S6-S7.) These analyses were performed after rapidly cooling the samples from these temperatures back to room temperature to capture the immediate thermal reactions without additional heat exposure. The NCM003 sample heated to 600 °C revealed the formation of interfacial domains approximately 10–20 nm thick, predominantly amorphous in nature, as depicted in Fig. 2c. Moreover, close to the NCM and LLTO boundary, reaction products were identified, including $LiTiO_2$ and $La_2Ti_2O_7$-like crystalline phase, as suggested by fast Fourier transformation (FFT) patterns (Fig. S8). The structural degradation of NCM and the formation of $LiTiO_2$ byproduct are also supported by additional HR-TEM analysis (Fig. S9). It infers the interface degradation through the decomposition of LLTO and NCM at this temperature. In the case of the NCM104 sample in Fig. 2d and Fig. S10-S11, byproducts such as $LiTiO_2$ and $LaTMO_3$ could be detected even after heating to lower temperature of 380 °C in the interfacial layer. This early degradation is consistent with the blurred interface observed at a similar temperature in the in situ heating TEM, indicating the vulnerability of the NCM104 open interface compared with the NCM003 closed interface. We further probed the co-sintering process particularly focusing on the local structure of NCM near the interface by nano-beam diffraction (NBD) analyses with a convergent beam area of ~ 4 nm in Fig. 2e, f. This investigation allowed us to measure the change in *d*-spacings for the (003) planes in NCM003 (marked with the red circle, (d_{003})) and the (104) planes in NCM104 (indicated with the blue circle, (d_{104})) throughout the heating process. A comparative analysis of d_{003} and d_{104} values in Fig. 2g, h, respectively, highlights the differences between the bulk domain and the interface domain as a function of temperature. It shows that, initially at low temperature, the d_{003} and d_{104} values at the interface align with those in the bulk. However, they begin to deviate significantly from the bulk values at elevated temperatures. Interestingly, each onset temperature of the deviation, approximately 600 °C for d_{003} and 400 °C for d_{104}, corresponds to the temperatures at which interfacial degradation was first observed. The decrease in d_{003} at the interface in NCM003 at high temperature is also consistent with the observed formation of disordered spinel-type NCM phase formed through phase transition from the layered structure in situ heating XRD, which is known to be typical with a delithiated layered material at high temperature, implying substantial lithium-ion diffusion from the cathode to the solid electrolyte[37–39]. In addition to the change in the structure of NCM, we also investigated the change in the structure of LLTO in aspect of a-lattice parameter using NBD analysis, as previously mentioned that Li-ion insertion into the LLTO accompanies the lattice expansion. The a-lattice parameters were extracted from the d-spacing of the (110) plane from the NBD patterns acquired at the LLTO interface. The results (Fig. S12) indicate that the a-lattice parameters in both NCM003 and NCM104 expand as the sintering temperature increases, implying Li-ion insertion into the LLTO.

The temperature-specific degradation was found to have a profound effect on the interfacial resistance (R_{int}) of NCM003 and NCM104 samples, as measured by the electrochemical impedance spectroscopy in Fig. 2i, j. To measure the R_{int}, the crystal orientation-controlled NCM/LLTO thin-film cells were fabricated with gold electrodes (See experimental sections for details). The interfacial resistance (R_{int}) of NCM003 starts to rise at 600 °C, and continues to increase at higher temperature. In contrast, the R_{int} of NCM104 begins to increase at 400 °C, but does not undergo significant further deterioration at elevated temperatures. These increases in the impedance correspond with the thermal reactions observed by in situ TEM at each respective onset temperature, suggesting that the structural collapse at the interface is a key factor in the surge of the interfacial resistance. Nevertheless, the different impedance behaviors of NCM003 and NCM104 at higher temperatures point to the distinct characteristics of their interfacial byproducts. It is supposed that the formation of an interphase in NCM104 at the early stage of the interfacial reaction could serve as a passivation layer, effectively limiting further increases in interfacial resistance, unlike the case of NCM003. This finding underscores a previously unrecognized link between the interfacial resistance

https://doi.org/10.1038/s41467-024-52226-4

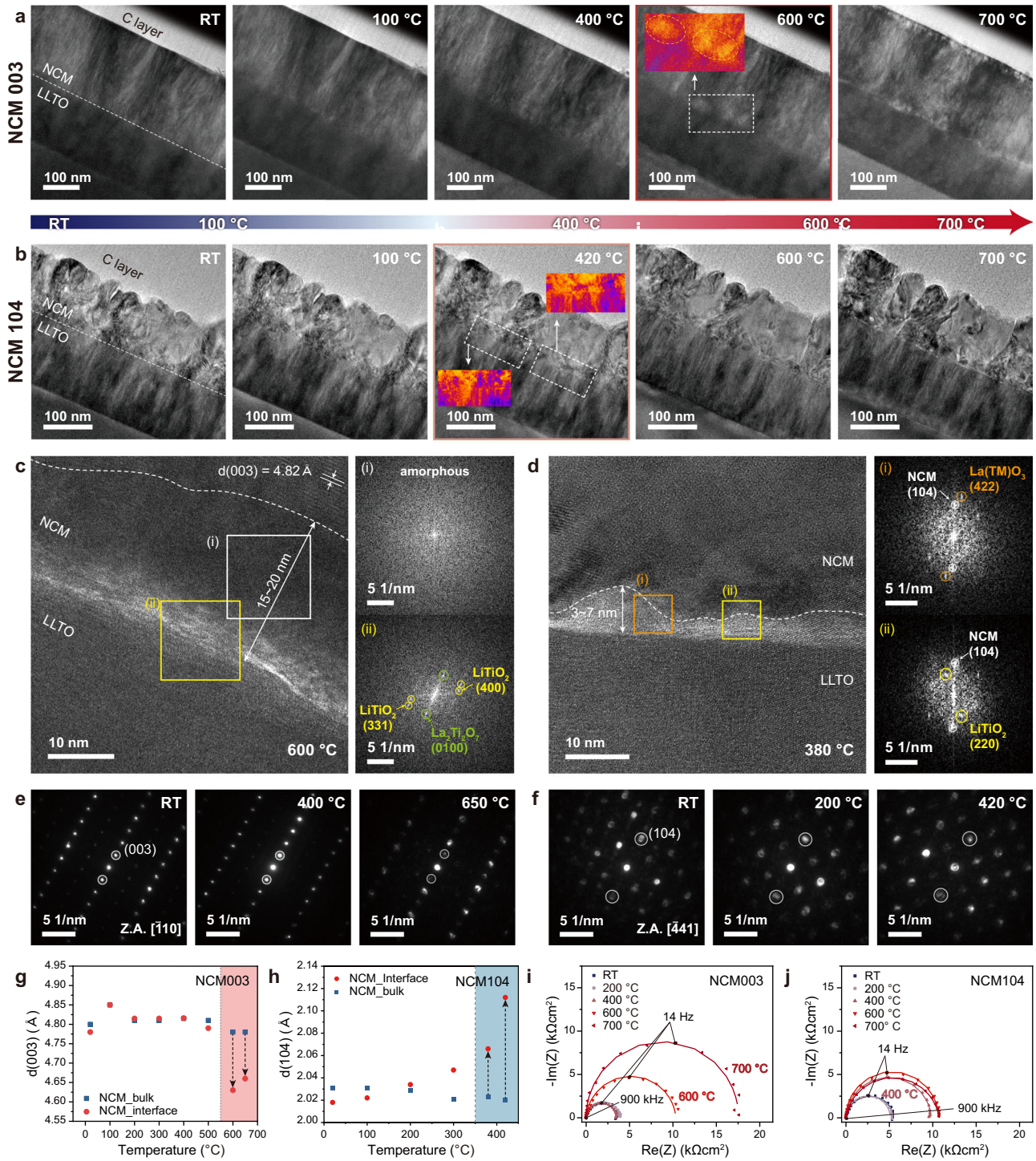

Fig. 2 | Structural evolution at different crystal-oriented interfaces during heating. In situ TEM snapshots during heating of NCM003 (**a**) and NCM104 (**b**). The morphological changes are observed at 600 °C and 420 °C in NCM003 and NCM104, respectively. Insets of (**a**) and (**b**) are color-coded images of white dashed boxes, showing contrast change in TEM images during in situ experiments. HR-TEM image of NCM003 heated at 600 °C (**c**) and NCM104 heated at 380 °C (**d**). Insets are the fast Fourier transform (FFT) patterns of marked regions with corresponding colors in the TEM image. Nano-beam diffraction (NBD) patterns at the interface during heating of NCM003 (**e**) and NCM104 (**f**). The plot for d-spacing of (003) in NCM003 (**g**) and d-spacing of (104) in NCM104 (**h**) as a function of temperature, measured at bulk and interface. Comparison of the electrochemical impedance spectroscopy (EIS) spectra of NCM003 (**i**) and NCM104 (**j**) at RT, 200 °C, 400 °C, 600 °C, and 700 °C.

and crystal orientation-dependent thermal reactions in composite cathodes. Moreover, they imply that the varying onset temperatures of thermal degradation reported in earlier studies of composite cathodes may have resulted from a mix of different reaction onsets across various crystallographic planes[17,19–21].

The origin of the different interfacial reaction pathway

In order to elucidate the origin of distinct impedance behaviors of NCM003 and NCM104, we further investigated how the phase evolution takes place by elemental and chemical analyses using electron energy loss spectroscopy (EELS), X-ray photoelectron spectroscopy

https://doi.org/10.1038/s41467-024-52226-4

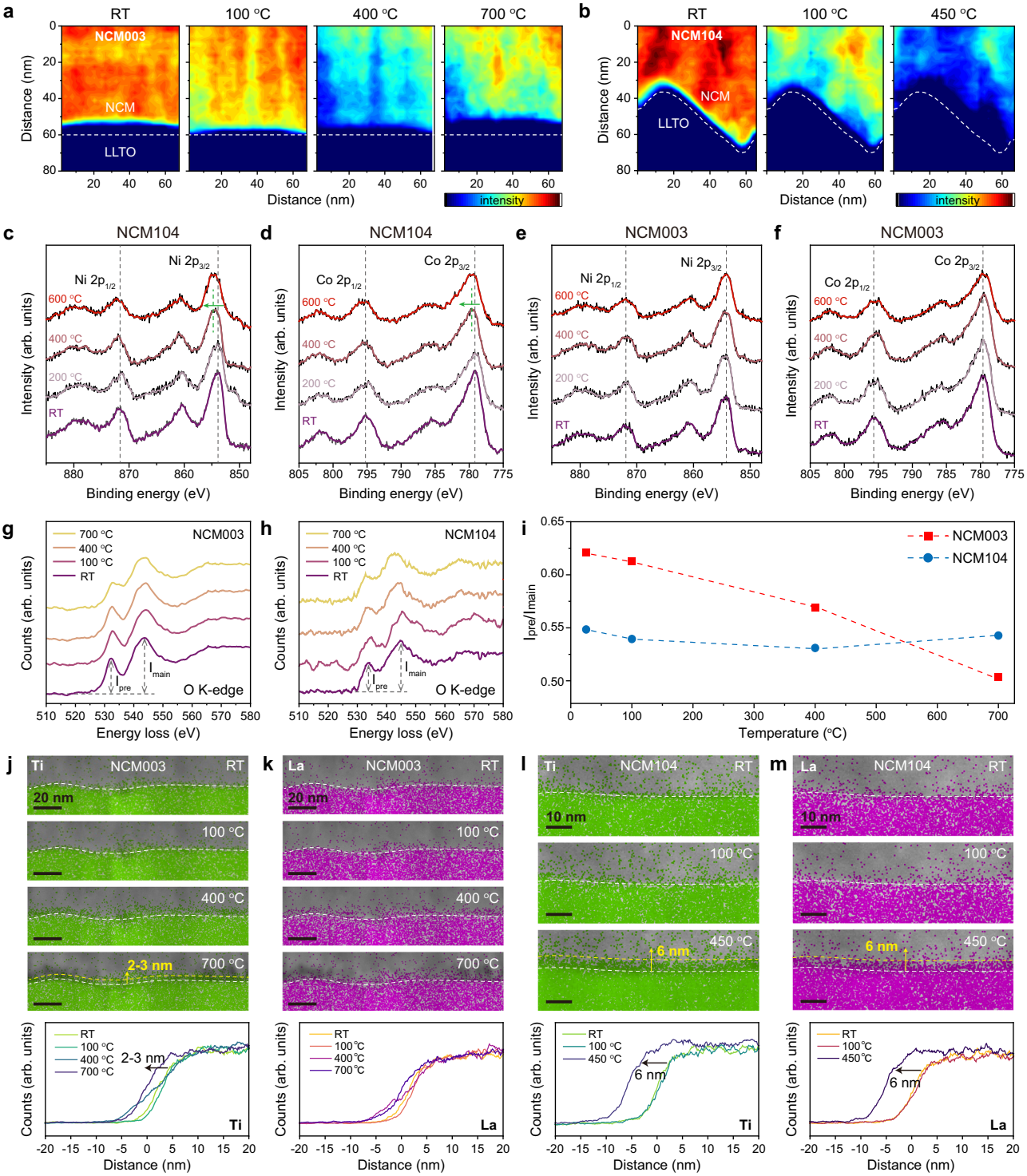

Fig. 3 | The change in the elemental distribution and chemical states at the cathode-electrolyte interface during heating. STEM images and corresponding Li EELS maps during heating of NCM003 (**a**) and NCM104 (**b**). White dotted lines in (**a**) and (**b**) indicate the interface lines between NCM and LLTO. XPS spectra of Ni *2p* (**c**) and Co *2p* (**d**) in NCM104, and Ni *2p* (**e**) and Co *2p* (**f**) in NCM003 with increasing annealing temperature. The green arrows indicate peak shifts of oxidation. EELS spectra of O K-edge in NCM003 (**g**) and NCM104 (**h**) during in situ heating. **i**. The change in the intensity ratio of I_{pre}/I_{main} in NCM003 and NCM104 as a function of temperature. EDS maps and profiles of Ti (**j**) and La (**k**) in NCM003, and Ti (**l**) and La (**m**) in NCM104 during in situ heating. The white dotted lines indicate the original boundary between NCM and LLTO at room temperature, and the yellow dotted lines indicate diffused front lines of respective elements.

(XPS), and energy dispersive spectroscopy (EDS). We first probed the lithium-ion re-distribution in NCM003 and NCM104 during heating, which are depicted by elemental EELS mapping in Fig. 3a, b, respectively. (The raw spectra of Li K-edge from the NCM interfaces at different temperatures are provided in Fig. S13.) In their pristine states, both NCM003 and NCM104 exhibit an explicit boundary between NCM and LLTO in the lithium intensity, featuring a steep concentration gradient. (More details on the pristine interface with STEM and

schematic images are provided in Fig. S14.) The boundary appears to be clear due to the lower lithium intensity in LLTO than in NCM, attributable to the higher lithium-ion concentration in NCM (49.3 mol L^{-1}) compared to LLTO (10.0 mol L^{-1}), as inferred from their crystallographic structure. As temperature rises, we observed a substantial reduction in lithium signal within the NCM regions for both samples, suggesting spontaneous lithium migration from NCM to LLTO, which is also supported by the a-lattice expansion of LLTO from 100 °C (Fig. S12), likely driven by the lithium concentration gradient between the two[17,19,20]. However, the amount of Li diffusion and pathway of lithium re-distribution varied between NCM003 and NCM104. For the NCM003 sample, noticeable lithium diffusion commenced around 400 °C, while in NCM104, a similar degree of lithium re-distribution is observable at around 100 °C. This discrepancy is attributed to the more favorable lithium migration in NCM104, facilitated by open ion diffusion channels allowing lithium-ions to move from NCM to LLTO more readily. It was also interesting to note that lithium diffusion took place in NCM003 only along certain lines penetrating through (003) plane, suggesting that these linear regions, possibly the crystalline imperfection such as grain boundaries, could act as diffusion paths at 400 °C. It contrasts to the case of NCM104, which displayed extensive diffusion through interfacial boundaries, likely due to the open ion channels toward the solid electrolyte. Noteworthy is that these significant lithium migrations have occurred at considerably lower temperatures (i.e., 400 °C for NCM003 and 100 °C for NCM104) than the onset temperatures of the interface degradations (i.e., 600 °C for NCM003 and 400 °C for NCM104), indicating that lithium re-distribution is a prerequisite for the interfacial reactions at higher temperature.

We found that the lithium re-distribution caused the change in the oxidation states of transition metals, as verified by the temperature-dependent XPS characterization. The XPS analysis, by performing depth profiling with ion-beam etching from NCM to LLTO in the epitaxial NCM/LLTO heterostructure, was conducted and plotted the XPS spectra from the interfacial region as a function of temperature in Fig. 3c–f and Fig. S15 [48–51]. Fig. 3c, d illustrate that both Ni 2*p* and Co 2*p* peaks shift to higher binding energy states during heating in NCM104 as indicated with dotted lines. It infers the oxidation of transition metals, which agrees with the extraction of lithium-ions from the NCM cathode as witnessed in lithium EELS mapping. On the other hand, the change in NCM003 was observed to be negligible, and both Ni 2*p* and Co 2*p* peaks did not display any noticeable shift as shown in Fig. 3e, f. Moreover, Fig. S15 revealed that even a slight reduction of Mn is detectable for NCM003 at 600 °C, indicating the overall reduction of the transition metals upon heating. The XPS results are further supported by EEL spectra of Mn L-edge, Co L-edge, and Ni L-edge, which are acquired in the NCM interfaces, as presented in Fig. S16. This observation is puzzling considering the apparent lithium extraction detected in EELS mapping at high temperature, even though the lithium re-distribution was less extensive in NCM003 than NCM104. We supposed that the reduction of the Mn state in NCM003 at high temperature could be related to the oxygen release, as previously reported for layered oxide cathodes with oxygen vacancies[52,53]. In this respect, we further assessed the extent of oxygen release by EELS O K-edge and probed the ratio of pre-peak and main peak (I_{pre}/I_{main}) at the NCM-side interface as a function of the temperature. It is known that the oxygen vacancy formation can be roughly estimated by the decrease in intensity of pre-edge for O K-edge[54,55]. Fig. 3g, h depict that the decrease in the pre-peak of O K-edge is evident in NCM003 particularly at high temperature. For the quantitative analysis, the I_{pre}/I_{main} ratio was calculated and plotted over the temperature in Fig. 3i. It discloses a significant drop of I_{pre}/I_{main} for NCM003 over temperature, which becomes the most dramatic at 700 °C, indicating the substantial oxygen release at high temperature. It contrasts to the case of NCM104 that maintains similar value of I_{pre}/I_{main} over temperature and suggests that the charge compensation primarily occurred through the oxygen loss in NCM003 at high temperature rather than the oxidation of transition metal. In addition to EELS O K-edge spectrum, we directly observed oxygen evolution in NCM003 by EDS and EELS mapping in Fig. S17. A lot of circular spots with darker contrast emerge at the NCM-side interface in NCM003 sintered to 700 °C, which can be correlated to circular areas with bright contrast of TEM images in Fig. 2a. The EELS O map shows that the regions with dark contrast have lower content of oxygen, which means that oxygen loss occurs within the regions. Given that the pristine NCM is stable at this temperature range[56], the premature oxygen release likely originates from the unstable characteristic of the interface, which involves the lithium-ion extraction from NCM and the oxygen-involving charge compensation in NCM003. Simultaneously, the absence of the oxygen loss at the same condition implies the relative stability of the interface for NCM104. We suppose that this stability is partly attributable to the facile migration of the cations (Ti and La) from the solid electrolyte through open channels in NCM104 and the effective charge compensation to suppress the oxygen-involving side reaction. As displayed in Fig. 3j, k, the cation migration is only minimally observed at the interface of NCM003 from the LLTO toward the NCM, both for Ti and La, which was found to diffuse by ~2 nm at 700 °C. In contrast, Ti and La in NCM104 could diffuse more extensively from LLTO to NCM as early as at 450 °C with thicknesses of ~6 nm (Fig. 3l, m), indicating the cation migration through the open channels could charge-compensate the lithium deficiency of NCM104 via interdiffusion. This observation suggests that cation interdiffusion, traditionally viewed as a contributor to interface instability, might also have beneficial roles. The high mobility of lithium can create a notable charge imbalance due to the preferential migration from the cathode to the electrolyte, especially at interfaces with closed pathways where the interdiffusion including high-valent cations such as La^{3+} or Ti^{4+} is limited. Such imbalances are likely to trigger oxygen-involved side reactions at the interface under elevated temperatures, leading to a substantial deterioration of interface integrity.

Proposed interface degradation mechanism in NCM/LLTO

Based on the findings, we propose crystal orientation-dependent interfacial degradation mechanisms during the co-sintering of the composite cathode in ASSBs, as illustrated in Fig. 4. When the cathode is in contact with the ion pathway facing the solid electrolyte, the open interface allows the lithium-ions in the cathode material to readily diffuse into the solid electrolyte starting from 100 °C. At 400 °C, the inter-diffusion of the Ti and La ions commences and the formation of the interphases appear as the main degradation product of the opened-interface system, leading to the increase of the interfacial resistance. However, further degradation of the interface is inhibited at a higher temperature owing to the formation of the interphases, which help the stability of the interface. On the other hand, when the ion pathway of the cathode is closed toward the solid electrolyte, the lithium-ion diffusion primarily takes place through the defective regions from the active material, thus is much less significant than that of the open ion pathway. In addition, due to the high kinetic barrier for ion transport especially for the high-valent ions, the inter-diffusion is suppressed, maintaining the low interfacial resistance without the formation of interphases up to a certain temperature. However, as the temperature rises over 600 °C, the significant one-way migration of cations results in the oxygen-evolving side reaction to charge compensate in wide regions of the interface, leading to an extensive deterioration of the interface. Considering the rapid interfacial resistance increase at 600 °C and further 700 °C, the structure degradation with oxygen release is supposed to be the most damaging and accelerates the interfacial degradation at higher temperature. These distinct temperature-dependent behaviors observed in NCM104 and NCM003 emphasize the importance of the interphase formation mechanism.

https://doi.org/10.1038/s41467-024-52226-4

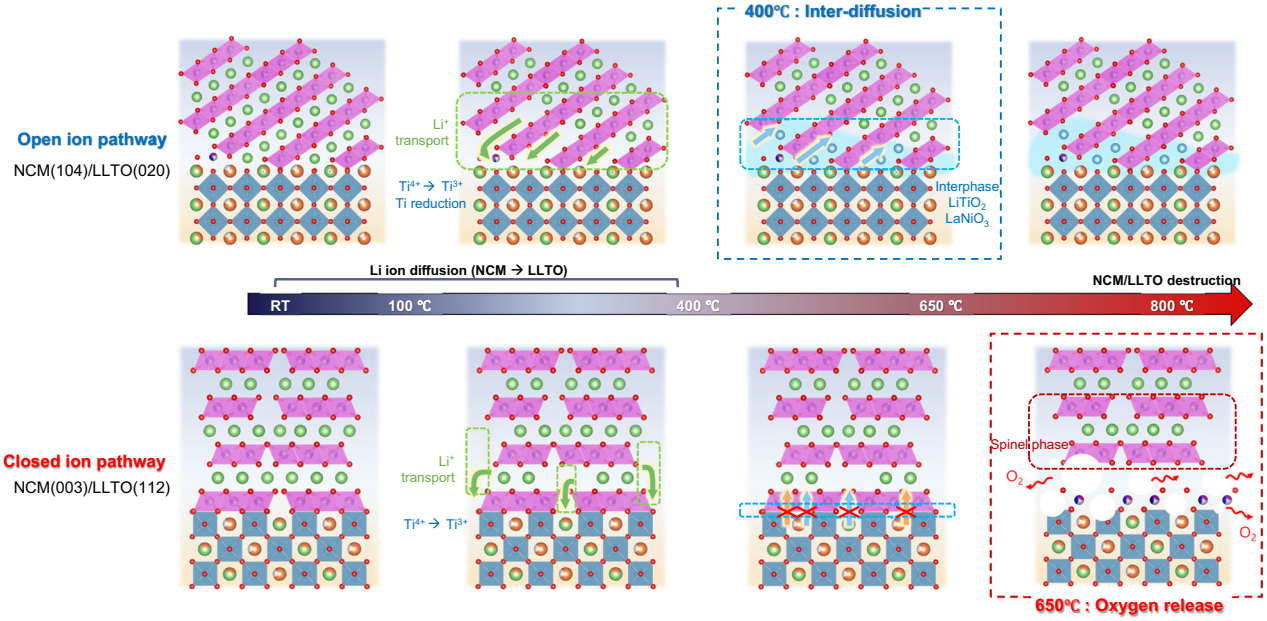

Fig. 4 | Proposed mechanisms of distinct interfacial reactions during the co-sintering of the composite electrode. The schematic illustrates the influence of the crystal orientation-dependent ion transport properties at the interface of NCM/LLTO on the interfacial reaction within the oxide-based composite cathode, as observed through in situ microscopic probe.

Conventional composite cathodes feature randomly oriented crystal facets that interface with each other, thus, the interfacial side reaction represents the cumulative effect of reactions at these individual interfaces (Fig. S18). Considering our findings about two representative interfacial systems, NCM003 and NCM104, we revisited the co-sintering process of the composite cathode comprising of polycrystalline NCM and LLTO particles with respect to the interfacial impedance during the heat treatment. The figure shows that the interfacial resistance in polycrystal NCM/LLTO increases slightly up to 400 °C, but it increases dramatically at over 600 °C. This is remarkably consistent with the findings that the early impedance increase is due to the formation of interphases from grains with open ion pathways, while the later upsurge is attributed to the oxygen-releasing deterioration of the grains with the closed ion pathway. This decoupled analysis may hint at a rational solution to effectively minimizing interfacial degradation of the composite cathodes during the co-sintering process. For example, to mitigate the major origin for the oxygen-releasing interface degradation, we may consider a surface coating of the oxygen-bond strengthening material such as Li_2TiO_3 (LTO) according to previous doping studies which reported strong Ti-O bond in layered cathode suppressing oxygen release[57,58]. Moreover, ensuring high ionic conductivity is equally important to maintain efficient lithium-ion transport[59,60], and LTO has been utilized as an effective coating species for cathode active materials due to relatively high lithium ionic conductivity of ~10^{-5} S cm^{-1} [58,61,62]. In our preliminary experiment, we could confirm that the oxygen gas evolution could be markedly suppressed in the Li_2TiO_3-coated NCM/LLTO with the simultaneous thermal analyzer-mass spectrometer (STA-MS) especially at temperatures above 500 °C (Fig. S19), See supplementary information for details). Subsequently, the overall resistance of the LTO-coated composite cathode could be substantially lowered after the co-sintering process, demonstrating the effectiveness of the strategy for suppressing oxygen release. These preliminary results support the idea that the fundamental understanding of individual interfacial properties and the thermal behavior is of the essence for the rational redesign of the composite cathodes for solid-state batteries.

Discussion

We investigated the effect of the crystal orientation at the interface on the interfacial reaction in the oxide-based composite cathode. Using the model system in which the crystal orientation is precisely controlled through epitaxial growths of electrode and solid electrolyte, we could directly observe that the interfacial reaction mechanism is highly dependent on the crystal orientation-dependent ion transport properties at the interface of NCM/LLTO using in situ analysis, with respect to the presence of open ion pathways. When the electrode is in contact with the ion pathway facing the solid electrolyte, it allows facile inter-diffusion of the lithium-ions and high-valent ions, promoting the formation of interphases which inhibit further degradation of the interface at high temperature. On the other hand, when the ion pathway is closed toward the solid electrolyte, the lithium-ion diffusion still takes place through the defective regions, however, due to the high kinetic barrier for the high-valent ions, the inter-diffusion is suppressed. Such imbalances trigger oxygen-involved side reactions at the interface under elevated temperatures, leading to an extensive deterioration of the interface. Based on this observation of distinct interfacial behaviors, we could decouple the complex interfacial impedance evolution of the conventional polycrystalline NCM/LLTO cathode composite. These fundamental understandings about the individual interfacial reaction involving interphase formation, oxygen evolution, and corresponding interfacial resistance provides fresh new insights into interfacial design between electrode and solid electrolyte, and our real-time probe of the well-defined interface is expected to open up a new possibility in further unraveling the complex interfacial properties in composite cathodes toward high-performance ASSBs.

Methods

Materials and epitaxial thin-film fabrication

The NCM powder was supplied by Samsung SDI and the LLTO powder was purchased from Toshima. The mixture powders were sintered at 600 °C with a ramping rate of 5 °C min^{-1} with the flowing argon gas. For the epitaxial growth of the NMC and LLTO, each material was deposited using the pulse laser deposition (PLD) method. A $SrTiO_3$ substrate (0.3905 Å similar to the lattice parameters of the two materials) was

used for epitaxial film growth. A laser with a wavelength of 248 nm using KrF medium gas was employed (COMPEX PRO 201 F, COHERENT), and the laser fluence was controlled at 2 J/cm^2. The growth temperature of each thin film was 400 °C and 650 °C, and the distance between the substrate and target was set to be 40 mm and 45 mm, respectively. The thickness of the film was controlled by rep rate and time, and the rep rate of each film was 5 Hz and 2 Hz. Under the same laser conditions, the $LaAlO_3$ layer, which was used as a current collector on the Nb-doped SrTiO3 substrate, was fabricated at the deposition temperatures of 600 °C.

Material characterizations

In situ heating XRD measurements were conducted in the 2θ range of 10–70° with a step size of 0.02° using an X-ray diffractometer (D8 Advance, Bruker) equipped with Cu Kα radiation (λ = 1.540598 Å) at the Research Institute of Advanced Materials at Seoul National University. In situ heating XRD data were obtained with Ar flowing at 2 ml min^{-1} while heating the samples at a ramping rate of 10 °C min^{-1} and resting for 1 h before the measurements at each given temperature. Ex situ powder X-ray diffraction patterns were obtained in the 2θ range of 10–70° with a step size of 0.02° using an X-ray diffractometer (New D8 Advance, Bruker). To probe the chemical evolution of the samples, XPS (Nexsa, Thermo Fisher Scientific installed at Korea institute of ceramic engineering and technology) analysis was conducted with an Al Kα radiation (1486.6 eV) and coupled with an Ar-ion etching for depth profile. All XPS spectra were calibrated based on the C 1 s at 284.5 eV. To detect the O_2 gas evolution of the annealed composite cathodes, the Simultaneous Thermal Analyser-Mass Spectrometer (STA 409 PC + QMS 403 C, NETZSCH installed at the Ajou University) was used with increasing temperatures up to 1000 °C under Ar flowing. The O_2 (m/z = 32) currents were normalized by the N_2 (m/z = 28) currents in order to exclude the effect of minor pressure and temperature changes.

In situ heating TEM experiments were performed using a commercially available holder and chips (DENSsolutions, Wildfire, Heating system). The electrodes were patterned on the chip near through-hole windows to generate a uniform heating environment. A two-dimensional lamella type of NCM | LLTO sample was manufactured using a focused ion beam (Thermo Fischer Helios G4 installed at the Korea Basic Science Institute) and loaded on the through-hole window of 5 μm diameter. The annealing temperature was ramped in stepwise with intervals of 20–30 °C as provided in Fig. S5 and in situ TEM movies were acquired using a dose rate of 200–300 e- Å^{-2} s^{-1}. In situ TEM experiments with HR-TEM imaging, NBD analysis, and EELS/EDS analysis were performed on a JEOL JEM 2100 F equipped with Gatan UltraScan 1000 operated at 200 kV, installed at the Institute for Basic Science (Seoul National University) and Cs-corrected JEOL ARM200F equipped with Gatan OneView camera at 200 kV, installed at the National Center for Inter-university Research Facilities (Seoul National University). STEM-EELS data were collected with a dispersion of 0.1 eV / 0.25 eV per channel for Li K-edge / O K-edge and a collection angle of 20.8 mrad using JEOL JEM 2100 F at 200 kV.

Cell fabrication and electrochemical measurements

The crystal orientation-controlled NCM/LLTO solid-state batteries were fabricated in the form of thin-film batteries. The electrically conductive Nb-doped $SrTiO_3$ was utilized as both a current collector and a substrate for epitaxial growth with the [001] and [111] orientations. $LaAlO_3$ thin layer with a few unit cells was deposited as a buffer layer to achieve an ohmic contact between NCM and Nb-doped $SrTiO_3$. The NCM and LLTO epitaxial thin films were deposited layer-by-layer on $LaAlO_3$/$SrTiO_3$ using the previously described epitaxial thin-film deposition technique. The gold layer as a current collector was deposited via the thermal evaporator. The galvanostatic EIS of the batteries was measured using a Bio-Logic SP 200 potentiostat/galvanostat by controlling the current with 10 nA at frequencies ranging from 3 MHz to 50 mHz. Without exposure to air, the electrochemical assessment of the batteries was conducted in a glove box.

Data availability

All relevant experimental data within the manuscript are available from the corresponding author upon reasonable request. Source data are provided in this paper.

References

1. Zahiri, B. et al. Revealing the role of the cathode–electrolyte interface on solid-state batteries. *Nat. Mater.* **20**, 1392–1400 (2021).
2. Manthiram, A., Yu, X. & Wang, S. Lithium battery chemistries enabled by solid-state electrolytes. *Nat. Rev. Mater.* **2**, 16103 (2017).
3. Yu, S. et al. Design of a trigonal halide superionic conductor by regulating cation order-disorder. *Science* **382**, 573–579 (2023).
4. Dai, T. et al. Inorganic glass electrolytes with polymer-like viscoelasticity. *Nat. Energy* **8**, 1221–1228 (2023).
5. Lee, Y.-G. et al. High-energy long-cycling all-solid-state lithium metal batteries enabled by silver–carbon composite anodes. *Nat. Energy* **5**, 299–308 (2020).
6. Kim, W. et al. Aging Property of Halide Solid Electrolyte at the Cathode Interface. *Adv. Mater.* **35**, 2301631 (2023).
7. Zhang, W. et al. Degradation Mechanisms at the Li10GeP2S12/LiCoO2 Cathode Interface in an All-Solid-State Lithium-Ion Battery. *ACS Appl. Mater. Interfaces* **10**, 22226–22236 (2018).
8. Jung, S.-K. et al. Pliable Lithium Superionic Conductor for All-Solid-State Batteries. *ACS Energy Lett.* **6**, 2006–2015 (2021).
9. Kim, K. J., Balaish, M., Wadaguchi, M., Kong, L. & Rupp, J. L. M. Solid-State Li–Metal Batteries: Challenges and Horizons of Oxide and Sulfide Solid Electrolytes and Their Interfaces. *Adv. Energy Mater.* **11**, 2002689 (2021).
10. Zhu, Y., He, X. & Mo, Y. Origin of Outstanding Stability in the Lithium Solid Electrolyte Materials: Insights from Thermodynamic Analyses Based on First-Principles Calculations. *ACS Appl. Mater. Interfaces* **7**, 23685–23693, (2015).
11. Kwon, W. J. et al. Enhanced Li+ conduction in perovskite Li3xLa2/3–x□1/3–2xTiO3 solid-electrolytes via microstructural engineering. *J. Mater. Chem. A* **5**, 6257–6262 (2017).
12. Allen, J. L., Wolfenstine, J., Rangasamy, E. & Sakamoto, J. Effect of substitution (Ta, Al, Ga) on the conductivity of Li7La3Zr2O12. *J. Power Sources* **206**, 315–319 (2012).
13. Yu, S. et al. Elastic Properties of the Solid Electrolyte Li7La3Zr2O12 (LLZO). *Chem. Mater.* **28**, 197–206 (2016).
14. Kim, Y. et al. The Effect of Relative Density on the Mechanical Properties of Hot-Pressed Cubic Li7La3Zr2O12. *J. Am. Ceram. Soc.* **99**, 1367–1374 (2016).
15. Kim, K. H. et al. Characterization of the interface between LiCoO2 and Li7La3Zr2O12 in an all-solid-state rechargeable lithium battery. *J. Power Sources* **196**, 764–767 (2011).
16. Kim, K. J. & Rupp, J. L. M. All ceramic cathode composite design and manufacturing towards low interfacial resistance for garnet-based solid-state lithium batteries. *Energy Environ. Sci.* **13**, 4930–4945 (2020).
17. Yu, C.-Y., Choi, J., Han, J., Lee, E. & Kim, J.-H. Phase Stability of Garnet Solid-Electrolyte Interfacing with Various Cathodes in All-Solid-State Batteries. *J. Electrochem. Soc.* **169**, 020520 (2022).
18. Liu, Y., Chen, J. & Gao, J. Preparation and chemical compatibility of lithium aluminum germanium phosphate solid electrolyte. *Solid State Ion.* **318**, 27–34 (2018).
19. Beaupain, J. P. et al. Reaction of Li1.3Al0.3Ti1.7(PO4)3 and LiNi0.6-Co0.2Mn0.2O2 in Co-Sintered Composite Cathodes for Solid-State Batteries. *ACS Appl. Mater. Interfaces* **13**, 47488–47498 (2021).
20. Yu, C.-Y., Choi, J., Anandan, V. & Kim, J.-H. High-Temperature Chemical Stability of Li1.4Al0.4Ti1.6(PO4)3 Solid Electrolyte with

Various Cathode Materials for Solid-State Batteries. *J. Phys. Chem. C.* **124**, 14963–14971 (2020).
21. Chandra, S. et al. Thermally-driven reactivity of Li0.35La0.55 TiO3 solid electrolyte with LiCoO2 cathode. *J. Mater. Chem. A* **10**, 3485–3494 (2022).
22. Stramare, S., Thangadurai, V. & Weppner, W. Lithium Lanthanum Titanates: A Review. *Chem. Mater.* **15**, 3974–3990 (2003).
23. Park, K. et al. Electrochemical Nature of the Cathode Interface for a Solid-State Lithium-Ion Battery: Interface between LiCoO2 and Garnet-Li7La3Zr2O12. *Chem. Mater.* **28**, 8051–8059 (2016).
24. Kim, Y. et al. Thermally Driven Interfacial Degradation between Li7La3Zr2O12 Electrolyte and LiNi0.6Mn0.2Co0.2O2 Cathode. *Chem. Mater.* **32**, 9531–9541 (2020).
25. Nishio, K. et al. Low resistance at LiNi1/3Mn1/3Co1/3O2 and Li3PO4 interfaces. *Appl. Phys. Lett.* **116**, 053901 (2020).
26. Nishio, K. et al. Impact of the Crystal Orientation of Positive Electrodes on the Interface Resistance across a Solid Electrolyte and Electrode. *ACS Appl. Energy Mater.* **3**, 6416–6421 (2020).
27. Hirayama, M. et al. Lithium intercalation in the surface region of an LiNi1/3Mn1/3Co1/3O2 cathode through different crystal planes. *RSC Adv.* **6**, 78963–78969 (2016).
28. Zhu, C. et al. Synergistic Effect of Microstructure Engineering and Local Crystal Structure Tuning to Improve the Cycling Stability of Ni-Rich Cathodes. *ACS Appl. Mater. Interfaces* **13**, 48720–48729 (2021).
29. Chemelewski, K. R., Shin, D. W., Li, W. & Manthiram, A. Octahedral and truncated high-voltage spinel cathodes: the role of morphology and surface planes in electrochemical properties. *J. Mater. Chem. A* **1**, 3347–3354 (2013).
30. Vardar, G. et al. Structure, Chemistry, and Charge Transfer Resistance of the Interface between Li7La3Zr2O12 Electrolyte and LiCoO2 Cathode. *Chem. Mater.* **30**, 6259–6276 (2018).
31. Miara, L. et al. About the Compatibility between High Voltage Spinel Cathode Materials and Solid Oxide Electrolytes as a Function of Temperature. *ACS Appl. Mater. Interfaces* **8**, 26842–26850 (2016).
32. Zhu, Y., He, X. & Mo, Y. First principles study on electrochemical and chemical stability of solid electrolyte–electrode interfaces in all-solid-state Li-ion batteries. *J. Mater. Chem. A* **4**, 3253–3266 (2016).
33. Bianchini, M. et al. The interplay between thermodynamics and kinetics in the solid-state synthesis of layered oxides. *Nat. Mater.* **19**, 1088–1095 (2020).
34. Park, H. et al. In situ multiscale probing of the synthesis of a Ni-rich layered oxide cathode reveals reaction heterogeneity driven by competing kinetic pathways. *Nat. Chem.* **14**, 614–622 (2022).
35. Ren, Y., Liu, T., Shen, Y., Lin, Y. & Nan, C.-W. Chemical compatibility between garnet-like solid state electrolyte Li6.75La3Zr1.75-Ta0.25O12 and major commercial lithium battery cathode materials. *J. Materiomics* **2**, 256–264 (2016).
36. Bak, S.-M. et al. Structural Changes and Thermal Stability of Charged LiNixMnyCozO2 Cathode Materials Studied by Combined In Situ Time-Resolved XRD and Mass Spectroscopy. *ACS Appl. Mater. Interfaces.* **6**, 22594–22601 (2014).
37. Hu, E. et al. Oxygen-Release-Related Thermal Stability and Decomposition Pathways of LixNi0.5Mn1.5O4 Cathode Materials. *Chem. Mater.* **26**, 1108–1118 (2014).
38. Bak, S.-M. et al. Correlating Structural Changes and Gas Evolution during the Thermal Decomposition of Charged LixNi0.8Co0. 15Al0.05O2 Cathode Materials. *Chem. Mater.* **25**, 337–351 (2013).
39. Hu, E. et al. Evolution of redox couples in Li- and Mn-rich cathode materials and mitigation of voltage fade by reducing oxygen release. *Nat. Energy* **3**, 690–698 (2018).
40. Zhang, L. et al. Lithium lanthanum titanate perovskite as an anode for lithium ion batteries. *Nat. Commun.* **11**, 3490 (2020).
41. Hua, C., Fang, X., Wang, Z. & Chen, L. Lithium storage in perovskite lithium lanthanum titanate. *Electrochem. Commun.* **32**, 5–8 (2013).
42. Van der Ven, A. Lithium Diffusion in Layered Li[sub x]CoO[sub 2]. *Electrochem Solid State Lett* **3**, 301 (1999).
43. Bates, J. B. et al. Preferred Orientation of Polycrystalline LiCoO[sub 2] Films. *J. Electrochem. Soc.* **147**, 59 (2000).
44. Li, Z. et al. Structural study of epitaxial LiCoO2 films grown by pulsed laser deposition on single crystal SrTiO3 substrates. *Thin Solid Films* **612**, 472–482 (2016).
45. Ulusoy, S., Gulen, S., Aygun, G., Ozyuzer, L. & Ozdemir, M. Characterization of thin film Li0.5La0.5Ti1−xAlxO3 electrolyte for all-solid-state Li-ion batteries. *Solid State Ion.* **324**, 226–232 (2018).
46. Wang, T. et al. Oriented Crystal Growth of La0.557Li0.330TiO3 in Bulk Ceramics Induced by LaAlO3 Single-Crystal Fibers. *Cryst. Growth Des.* **21**, 2093–2100 (2021).
47. Fourquet, J. L., Duroy, H. & Crosnier-Lopez, M. P. Structural and Microstructural Studies of the Series La2/3−xLi3x□1/3−2xTiO3. *J. Solid State Chem.* **127**, 283–294 (1996).
48. Yang, K.-Y., Fung, K.-Z. & Wang, M.-C. X-ray photoelectron spectroscopic and secondary ion mass spectroscopic examinations of metallic-lithium-activated donor doping process on La0.56Li0.33TiO3 surface at room temperature. *J. Appl. Phys.* **100**, 056102 (2006).
49. Shi, Y., Chen, G., Liu, F., Yue, X. & Chen, Z. Resolving the Compositional and Structural Defects of Degraded LiNixCoyMnzO2 Particles to Directly Regenerate High-Performance Lithium-Ion Battery Cathodes. *ACS Energy Lett.* **3**, 1683–1692 (2018).
50. Chen, Z. et al. Hierarchical Porous LiNi1/3Co1/3Mn1/3O2 Nano-/Micro Spherical Cathode Material: Minimized Cation Mixing and Improved Li+ Mobility for Enhanced Electrochemical Performance. *Sci. Rep.* **6**, 25771 (2016).
51. Amine, K., Tukamoto, H., Yasuda, H. & Fujita, Y. A New Three-Volt Spinel Li1 + x Mn1.5Ni0.5 O 4 for Secondary Lithium Batteries. *J. Electrochem. Soc.* **143**, 1607 (1996).
52. Qiu, B. et al. Gas–solid interfacial modification of oxygen activity in layered oxide cathodes for lithium-ion batteries. *Nat. Commun.* **7**, 12108 (2016).
53. Li, M. et al. Cationic and anionic redox in lithium-ion based batteries. *Chem. Soc. Rev.* **49**, 1688–1705 (2020).
54. Yang, L. et al. Direct View on the Origin of High Li+ Transfer Impedance in All-Solid-State Battery. *Adv. Funct. Mater.* **31**, 2103971 (2021).
55. Wang, Z. et al. In Situ STEM-EELS Observation of Nanoscale Interfacial Phenomena in All-Solid-State Batteries. *Nano Lett.* **16**, 3760–3767 (2016).
56. Sicklinger, J., Metzger, M., Beyer, H., Pritzl, D. & Gasteiger, H. A. Ambient Storage Derived Surface Contamination of NCM811 and NCM111: Performance Implications and Mitigation Strategies. *J. Electrochem. Soc.* **166**, A2322–A2335 (2019).
57. Cheng, Y. et al. Stabilizing effects of atomic Ti doping on high-voltage high-nickel layered oxide cathode for lithium-ion rechargeable batteries. *Nano Res.* **15**, 4091–4099 (2022).
58. Wang, J. et al. Improving the electrochemical properties of LiNi0.5Co0.2Mn0.3O2 at 4.6 V cutoff potential by surface coating with Li2TiO3 for lithium-ion batteries. *Phys. Chem. Chem. Phys.* **17**, 32033–32043 (2015).
59. Zhong Y. et al. Understanding and unveiling the electro-chemo-mechanical behavior in solid-state batteries. *SusMat.* **4**, e190 (2024).
60. Tan, D. H. S. et al. From nanoscale interface characterization to sustainable energy storage using all-solid-state batteries. *Nat. Nanotechnol.* **15**, 170–180 (2020).
61. Li, Y. et al. One-Step Synthesis of a Nanosized Cubic Li2TiO3-Coated Br, C, and N Co-Doped Li4Ti5O12 Anode Material for Stable High-Rate Lithium-Ion Batteries. *ACS Appl. Mater. Interfaces* **11**, 25804–25816 (2019).
62. Meng, K., Wang, Z., Guo, H., Li, X. & Wang, D. Improving the cycling performance of LiNi0.8Co0.1Mn0.1O2 by surface coating with Li2TiO3. *Electrochim. Acta* **211**, 822–831 (2016).

Acknowledgements
This work was supported by SAIT, Samsung Electronics Co., Ltd. This work was also supported by the Institute for Basic Science (IBS-R006-D1), the Defense Challengeable Future Technology Program of the Agency for Defense Development, Republic of Korea (Contract Number: UC190025RD) and the National Research Foundation of Korea (NRF) grant funded by the Korea government (2021M3H4A1A04093050). This research was supported by Basic Science Research Program through the National Research Foundation of Korea(NRF) funded by the Ministry of Education(2022R1A6A3A13057054). H.P., J.K., and J.P. acknowledge the National Research Foundation of Korea (NRF) grant, funded by the Korea government (MSIT) (No. NRF-2017R1A5A1015365) and Samsung Research Funding & Incubation Center for Samsung Electronics (Project Number SRFC-MA2002-03).

Author contributions
S.L. and H.P. contributed equally to this work. S.L. and H.P. designed the experiment, conducted the measurement, analyzed the data and prepared the manuscript. J.Y.K. and M.C. conducted the fabrication of the materials, while H.P. and J.K. performed the in situ TEM test. S.H., S.K., W.K., and H.W.J. offered valuable comments and discussion on the experimental design and analyses. K.K. and J.P. supervised the project and co-contributed to the experimental planning, data analysis and manuscript preparation.

Competing interests
The authors declare no competing interests.

Additional information
Supplementary information The online version contains supplementary material available at https://doi.org/10.1038/s41467-024-52226-4.

Correspondence and requests for materials should be addressed to Jungwon Park or Kisuk Kang.

Peer review information *Nature Communications* thanks Xuelong Wang and the other, anonymous, reviewers for their contribution to the peer review of this work. A peer review file is available.